Journal of Energy

VOLUME 75 Number 3 | 2026

journal homepage: http://journalofenergy.com/

Impact of Alternative Dielectric Liquids on UHF Partial Discharge Signal Propagation and Source Localization in Power Transformers

Djordje Dukanac

***Summary* —This paper presents Ansys HFSS simulation results for two power transformer models filled with different liquid dielectrics: mineral oil (MO) and natural ester (NE). Equipped with a partial discharge (PD) source and four ultra-high frequency (UHF) sensors, these models provide highly relevant data for improving PD diagnosis and localization. The study analyzes the first peaks (FPs), extreme amplitudes (EAs), initial delays, waveforms, weighted mean amplitudes, and weighted mean frequency shifts of the UHF PD signals to evaluate the effects of different propagation paths and attenuation levels within the two dielectric liquids. These parameters are captured by the four UHF sensors during a 12.179 ns window following the FPs, as well as over a longer period extending from the FPs until the end of the 45 ns recording. Furthermore, the FP method is applied to determine and explain why the calculated PD source locations differ between the two liquid dielectric scenarios. The study also examines how waves reflected from internal metal components affect the signals received by the sensors. On average, the FPs and EAs in the first wave packets of Signals 1–4 are 1.85 and 1.28 times larger, respectively, in the NE model than in the MO model. When using identical dipole antennas for both the source and sensors, the frequency ratio between the peaks of the radiated or accepted power curves for MO and NE is 1.198. Finally, utilizing the transformer model with NE increases the average PD source location error by 1.017 mm compared to the model with MO.**

***Keywords* — Dielectric liquids, Extreme amplitude, First peak, Mineral oil, Natural ester, Partial discharge localization, Power transformer, Ultra-high frequency (UHF) sensors.**

I. Introduction

The security and reliability of the electrical power supply heavily depend on the dependable operation of power transformers within the electrical grid. When high electric field stresses are applied to a dielectric material inside a transformer, the material undergoes a localized dielectric breakdown. This results in a low-intensity electrical discharge known as a partial discharge (PD). Such discharges can be initiated by natural insulation aging, manufacturing defects that provoke early failures, sustained operational overvoltages, or transient overvoltages caused by switching operations and lightning strikes [1], [2].

Predictive maintenance entails monitoring PD activity levels within transformers to identify internal faults before severe damage occurs. Furthermore, precisely localizing the PD source inside power transformers is crucial for operational risk analysis, maintenance scheduling, and overall repair efficiency.

The ultra-high-frequency (UHF) approach offers several advantages, including continuous online monitoring, a high signal-to-noise ratio, robustness against external disturbances, and the ability to locate PD sources in three dimensions [3], [4].

In [5], a localization methodology combining Dijkstra's algorithm with an artificial neural network (ANN) was developed and evaluated using a 3D CAD model of a 300 MVA transformer (900 cm × 400 cm × 260 cm). To validate the approach, localization errors derived from the proposed algorithm were compared against experimental and simulation results utilizing four UHF sensors.

In [6], a deep learning (DL)-based method for the 3D localization of PDs was developed using a three-sensor configuration. The robustness of the framework was evaluated across three distinct transformer tank volumes: 1000 × 1000 × 500 mm³, 500 × 1000 × 500 mm³, and 2000 × 1000 × 1000 mm³.

In [7], the authors simulated a validated model of a three-phase, 300 MVA, 420 kV power transformer with artificial PD sources inside the winding. The study aimed to identify the exact tank wall locations where UHF sensors could detect these internal PD pulses with the highest sensitivity.

Due to fewer physical obstacles in the simulation model, the distance-dependent attenuation reported in [8] was lower than that of the 300 MVA, 420 kV transformer experimental setup. Nevertheless, both models exhibited similar attenuation characteristics.

In [9], the simulated time-domain electromagnetic (EM) waveforms, their frequency spectra, and the attenuation characteristics of the EM waves as they propagated through transformer windings or inside the tank showed good agreement with experimental results.

The propagation delay of the PD signal from each location within the 3D space comprised by the transformer model to the UHF sensors was initially determined in [10]. Using a binary particle swarm optimization algorithm, the propagation delays of the simulated and measured signals were compared, identifying the PD location as the point where the simulated propagation times most

(Corresponding author: Djordje Dukanac)

Djordje Dukanac is with Joint-Stock Company Elektromreža Srbije, Belgrade, Serbia

(email: djdukanac@gmail.com)

Djordje Dukanac, Impact of Alternative Dielectric Liquids on UHF Partial Discharge Signal Propagation and Source Localization in Power Transformers, Journal of Energy, vol. 75 Number 3 (2026), 74–84
https://doi.org/10.37798/2026753790

© 2026 Copyright for this paper by authors. Use permitted under Creative Commons Attribution-NonCommercial (CC BY-NC) 4.0 International License

closely match the measured data.

In [11], Dijkstra's shortest path algorithm is utilized to find the optimal match between the measured signals and the database data. In-service transformers lack the detailed internal component data required for database construction. To overcome this, the hyperbolic approach is solved using three distinct methods: an iterative algorithm, the Fang method, and the Chan method. The same 230/69 kV, 180 MVA oil-filled power transformer from [10] was utilized. Simulations for [6]–[10], and [11] were carried out using CST Microwave Studio software.

A research method for detecting UHF PDs via transformer iron core induction signals is presented in [12]. Alongside a finite-difference time-domain (FDTD) simulation analyzing signal propagation, enhancement, and extraction, the approach was experimentally validated using a 110 kV single-phase dual-winding transformer.

To eliminate non-convergence issues, reference [13] proposes a time difference of arrival (TDOA) database-based solution for PD source localization. The authors modeled the transformer structure with simplified barriers using Helix 3D and Microsoft Windows Presentation Foundation (.NET WPF), validating the approach through two distinct experiments: one utilizing a 110 kV power transformer and another using a dedicated PD testing platform for electric power equipment.

In [14], the feasibility of locating a PD source inside the windings via UHF methods was investigated by using XFDTD software to simulate wave propagation through the windings to the sensor, while analyzing the cause of arrival time delay with a geometric model. To evaluate the technique's measurement sensitivity and localization accuracy, a 220 kV oil-immersed transformer equipped with four UHF sensors was utilized.

In [15], a transformer simulation model featuring an acceptable simplification of the core and windings was presented. Utilizing the FDTD method to simulate EM wave propagation, the authors reported on how different sizes of the core and windings alter the PD signal waveforms. Using a Hilbert fractal antenna, experimental PD tests were conducted on two types of artificial oil-paper insulation defects in a simulated transformer tank containing the core and windings to validate the simulation model.

In [16], UHF signal propagation within a power transformer was simulated and demonstrated at four distinct time intervals. Subsequently, a bio-inspired UHF sensor for PD detection was designed, fabricated, and experimentally validated using a dedicated laboratory setup.

When at least four UHF sensors are installed through the transformer tank wall—typically via the oil drain valve or a specialized dielectric window—the TDOAs between the signals can be utilized to localize the PD source [17], [18]. However, as the PD signal travels from its source to the sensors, its energy and waveform characteristics are significantly influenced by the internal transformer components and the exact propagation distance [19], [20].

In this paper, typical power transformer models are developed using Ansys HFSS software. The software employs the finite element method (FEM) to analyze PD signals received by four UHF sensors, allowing the PD source to be located via the first peak (FP) method. Two dielectric media are considered: natural ester (NE) and mineral oil (MO). The simulation setup and its limitations are presented in Section II. Simulation results for various electrical dielectric liquids are analyzed and discussed in Section III. This section thoroughly compares the significant signal characteristics at the PD source and UHF sensors, alongside the calculated positions of the PD source within the MO and NE transformer models. Section IV discusses the physical mechanisms governing UHF PD wave propagation and evaluates how dielectric liquid properties dictate sensor responses. Section V summarizes the paper's most significant data and primary conclusions.

II. Simulation Setup

The simulation model incorporates a three-phase power transformer rated at 66/11 kV and 5 MVA. Housed within a (2300 x 880 x 2800 mm) tank alongside the magnetic core and three-phase windings are five dipole antennas, configured as four UHF sensors and one PD source. Two distinct models are obtained by varying the dielectric liquid medium.

A. Power Transformer Simulation Setup

The typical structural configuration of the power transformer is illustrated in Figure 1a, comprising:

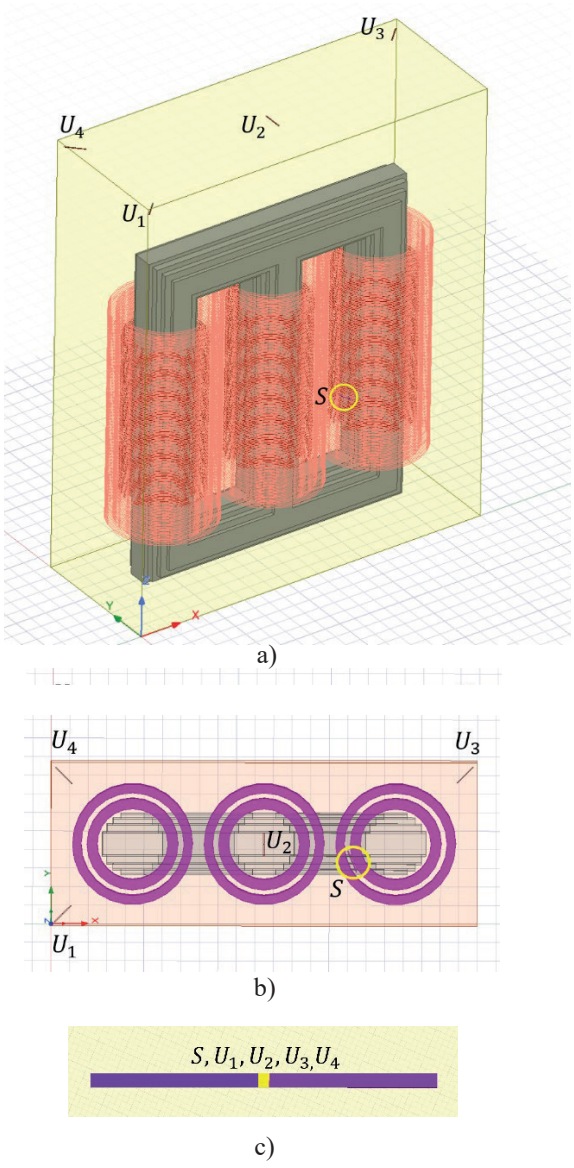

Fig. 1. Power transformer simulation model comprising a metal tank, three-phase windings, and a three-limb magnetic core under different dielectric fluids (MO or NE): a) side view, b) top view, and c) dipole antenna configuration used for the UHF sensors (U1, U2, U3, and U4) and the PD source (S).

Djordje Dukanac, Impact of Alternative Dielectric Liquids on UHF Partial Discharge Signal Propagation and Source Localization in Power Transformers, Journal of Energy, vol. 75 Number 3 (2026), 74–84
https://doi.org/10.37798/2026753790
© 2026 Copyright for this paper by authors. Use permitted under Creative Commons Attribution-NonCommercial (CC BY-NC) 4.0 International License

- A 304 stainless steel tank
- A dielectric liquid medium (MO or NE)
- A three-limb, four-stage, seven-step magnetic core
- Three-phase low-voltage (LV) windings
- Three-phase high-voltage (HV) windings

The PD source is positioned at coordinates *S* (1625, 340, 825) mm. Geometrically, this location corresponds to the gap between the upper section of the 13th disc of the HV winding's lower half and the lower section of the 10th disc of the LV winding. Both windings are wound around the third core limb. Relative to the transformer layout shown in Figure 1a, the source is located within the right core window, shifted slightly toward the foreground.

The side and top views of the simulation model are illustrated in Figures 1a and 1b, respectively, where MO and NE are independently utilized to establish two distinct dielectric models. The designated spatial positions (centers of symmetry) for the four receiving UHF sensors are defined as: U_1 (65, 65, 2750) mm, U_2 (1150, 440, 2758) mm, U_3 (2235, 815, 2755) mm, and U_4 (70, 810, 2760) mm. Figure 1c shows the specific dipole antenna configuration implemented for both the PD source and the UHF sensors, featuring copper arms that measure 60 x 5 mm. For instance, the maximum distance between the farthest points inside the empty transformer tank is 3728.86 mm. This distance translates to an EM wave delay of 18.436 ns in MO and 22.235 ns in NE, assuming a relative dielectric permittivity of 2.2 and 3.2, respectively.

B. Model Limitations and Approximations

The specific properties assigned to NE and MO were selected from established literature, namely: relative permittivity (3.2 vs. 2.2), bulk conductivity (4.31 × 10^{-10} S/m vs. 6.25 × 10^{-10} S/m), dielectric loss tangent (0.0036 vs. 0.003), and mass density (920 kg/m³ vs. 890 kg/m³).

To accommodate hardware constraints and software limits within Ansys HFSS, the three-phase LV and HV winding geometries were simplified relative to the manufacturer's original design. Excessively detailed models significantly escalate computational overhead, often leading to simulation non-convergence or execution failures due to insufficient memory and processing capacity.

The relative permittivity of the three-phase winding insulation is assumed to approximate that of the liquid dielectric (MO or NE). This is because the paper insulation is fully impregnated, which effectively lowers its overall permittivity. Since the pressboard insulation layers are fully impregnated with the dielectric liquid, effectively reducing their relative permittivity, the inter-winding insulation between the LV and HV windings is assumed to approximate that of the fluid itself (MO or NE).

The LV and HV windings consist of 42 discs of appropriate geometric dimensions. The winding copper is approximated as a perfect electrical conductor (PEC). The 1.2 mm thick intermediate insulation between adjacent LV or HV radial disc coils is omitted from the model and replaced with a continuous PEC boundary. Each HV disc is simplified into two parts separated by a 1.2 mm gap, rather than comprising four vertical sections. At an operating frequency of 1 GHz, where the wavelengths in MO and NE are 20.23 cm and 16.77 cm, respectively, this 1.2 mm aperture is electrically small. Consequently, these wavelengths become progressively larger at lower frequencies. Aperture diffraction causes the signal passing through this small opening to scatter widely rather than remaining directional. This scattering effectively reduces the wave's power density along the shortest geometric path to the receiving UHF sensor.

The following minor components are excluded from the power transformer simulation model due to a lack of precise design data and to prevent unnecessary geometric complexity: a) auxiliary insulation elements, including spacers, tapes, and sleeves; and b) mechanical fixing components, winding clamping structures, winding output leads, bolts, and metal core clamping frames.

C. Modeling and Characteristics of the PD Source and UHF Sensors

As illustrated in Figure 2a, the dipole antenna from Figure 1c is enclosed within a 500 mm cubic radiation boundary filled with either MO or NE to evaluate its characteristics. The antenna's center of symmetry is positioned at coordinates (250, 250, 250) mm relative to the Cartesian origin. The PD excitation source is modeled as a broadband pulse spanning 0 to 1 GHz, with an input power of 1 W and a peak amplitude of 1 V.

For the cube filled with MO or NE containing the centered antenna, Figure 2b displays the transmitting antenna's radiated power and accepted power against frequency. It is evident that in both scenarios, the radiated power curve sits slightly below the accepted power curve. The dipole antenna's power curves reach their maxima at 630 MHz for NE and 755 MHz for MO. At these respective peaks, the maximum radiated power is 4.58% and 3.62% lower than the maximum accepted power.

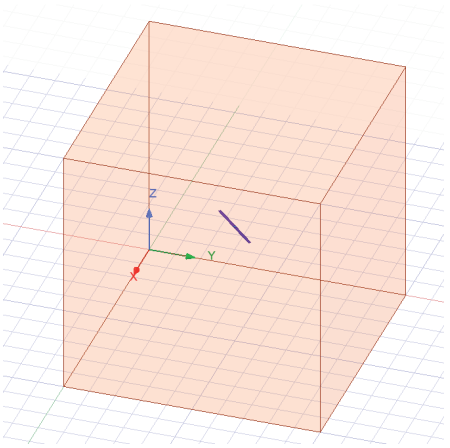

a)

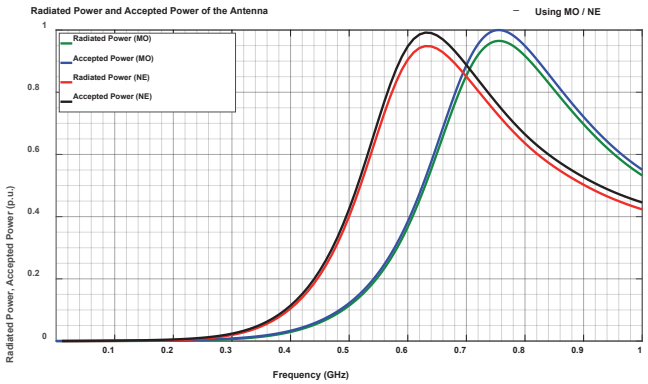

b)

Fig. 2. a) UHF dipole antenna positioned at the center of a 500 mm cubic domain bounded by radiation boundaries and filled with MO or NE. b) Radiated and accepted power versus frequency for the two dielectric media.

Djordje Dukanac, Impact of Alternative Dielectric Liquids on UHF Partial Discharge Signal Propagation and Source Localization in Power Transformers, Journal of Energy, vol. 75 Number 3 (2026), 74–84
https://doi.org/10.37798/2026753790
© 2026 Copyright for this paper by authors. Use permitted under Creative Commons Attribution-NonCommercial (CC BY-NC) 4.0 International License

At an operating frequency of 1 GHz, the far-field 3D polar diagrams and 2D rectangular contours of the realized gain (dB) for the center-positioned dipole antenna are displayed in Figures 3 and 4. Specifically, Figures 3a and 4a illustrate the antenna characteristics in MO, while Figures 3b and 4b show the corresponding performance in NE. Across all visualizations, the realized gain scales from minimum to maximum along a blue-to-red color gradient.

Figures 3a and 3b illustrate that the realized gain pattern of the transmitting dipole antenna is non-omnidirectional. The 3D radiation profile exhibits a quasi-cubic rather than a spherical geometry. In the x-y plane, the realized gain reaches its minimum along the longitudinal axis of the UHF transmitting antenna, remaining low within approximately ±50° of its center. Similarly, the x-z plane radiation pattern shows minimum intensity along the vertical z-axis of the antenna's center of symmetry, spanning a low-gain region of ±12°. Consequently, these quasi-rectangular 3D polar diagrams concentrate their peak realized gain intensities along their four narrowest lateral faces.

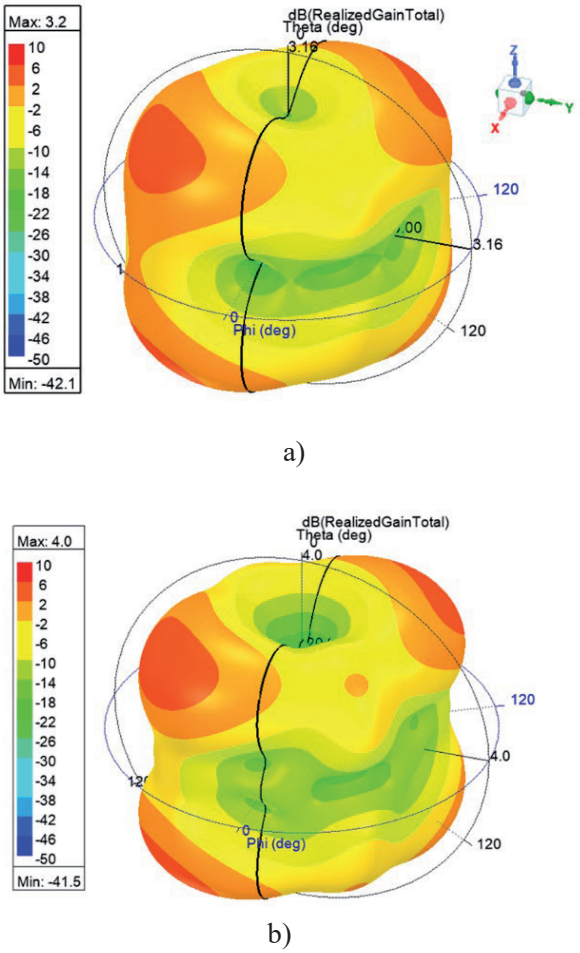

Fig. 3. 3D far-field realized gain polar diagrams [dB] of the dipole antenna centered within a 500 mm cubic enclosure with transparent walls, immersed in: a) MO and b) NE.

Compared to the NE cube (Figure 4b), the MO cube (Figure 4a) features a 33% narrower central region of decreased realized gain, yet delivers up to 30.76% higher gain within that specific zone. Conversely, the NE cube achieves a maximum realized gain of 3.96 dB. This is 25.32% higher than the MO cube's peak, with both maximums located on the shorter peak sides of the 3D plots in Figures 3a and 3b, respectively.

Due to antenna reciprocity, the spatial distribution of the realized gain for both dielectric liquids remains identical during UHF signal transmission and reception.

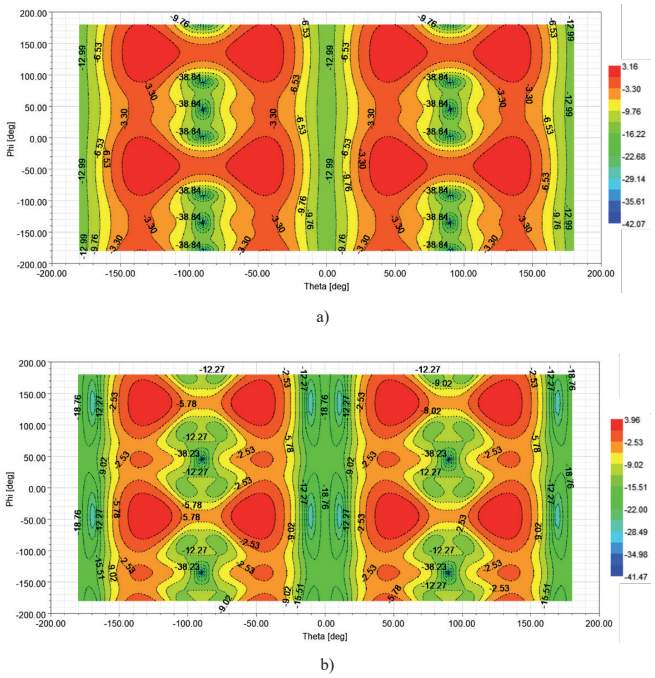

Fig. 4. 2D far-field rectangular contours of the realized gain (dB) for a dipole antenna centered within a 500 mm cubic enclosure with electromagnetically transparent walls, filled with: a) MO and b) NE.

III. Simulation Results and Analysis for Two Dielectric Liquids

This section evaluates the simulation results for the MO and NE dielectric liquids utilizing the power transformer model from Figure 1a. The analysis is structured across four subsections: Subsection A examines the input pulses and output signals of the transmitting antenna (PD source), while Subsections B and C analyze the signal waveforms and frequency spectra of the receiving UHF sensors, respectively. Finally, Subsection D presents a comparative assessment of the PD source localization error for both liquids.

A. Input Pulses and Output Signals of the PD Source Antenna

Figure 5a displays the transmitting antenna's input pulses and output signals for both MO and NE within the transformer model. The inputs are modeled as Gaussian PD pulses with a 1V amplitude and a frequency range of 0 to 1 GHz. Because the input conditions are uniform, these pulses overlap perfectly and are virtually identical. Conversely, the antenna output signals for both MO and NE exhibit oscillatory behavior with a significantly longer duration than the input pulses. Their first pulses are broader, featuring peak delays that are 1.14 and 1.35 times longer, and peak amplitudes that are 1.23 and 1.38 times lower than their respective inputs. While the output signals for both liquids initiate simultaneously, the MO signal gradually lags behind the NE response over time.

Figure 5b illustrates the amplitude spectra computed over the [0.534–3.162] ns time interval. All spectral curves converge to identical amplitudes at approximately 165 MHz and 1 GHz. While the input pulse spectra nearly overlap across the entire band, the output signal spectra exhibit liquid-dependent dielectric effects. Specifically, the NE output spectrum remains lower than all other curves within the [165–1000] MHz range. In contrast, the MO output spectrum drops below the input pulse baselines only within the [463–1000] MHz frequency band.

Djordje Dukanac, Impact of Alternative Dielectric Liquids on UHF Partial Discharge Signal Propagation and Source Localization in Power Transformers, Journal of Energy, vol. 75 Number 3 (2026), 74–84
https://doi.org/10.37798/2026753790
© 2026 Copyright for this paper by authors. Use permitted under Creative Commons Attribution-NonCommercial (CC BY-NC) 4.0 International License

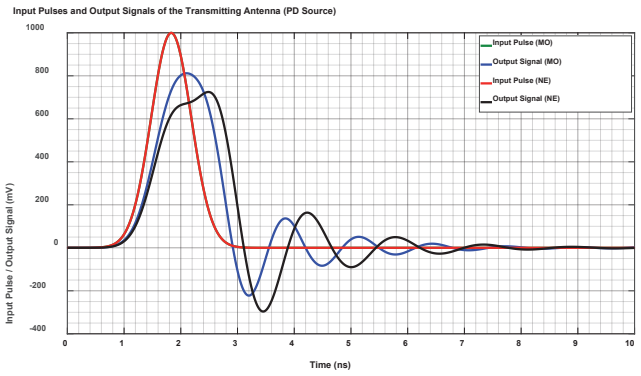

a)

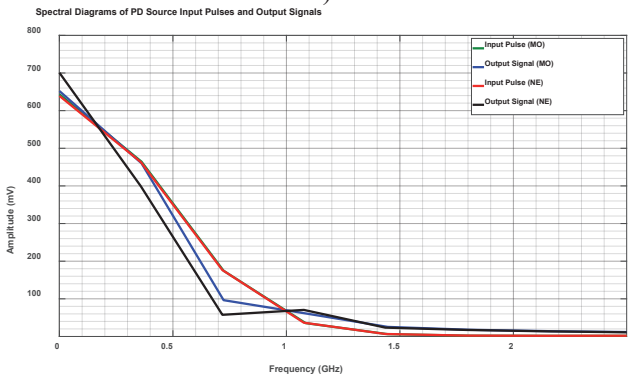

b)

Fig. 5. Transmitting antenna signals for MO- and NE-filled transformer models: a) input Gaussian PD pulses and corresponding output waveforms; b) amplitude spectra of the input pulses and output signals.

B. Output Signals Recorded at UHF Sensors 1–4

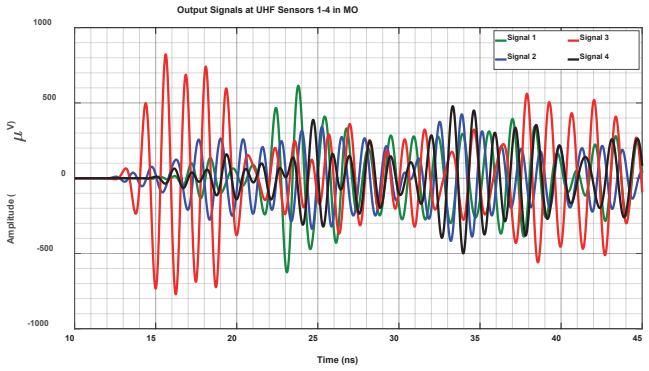

a)

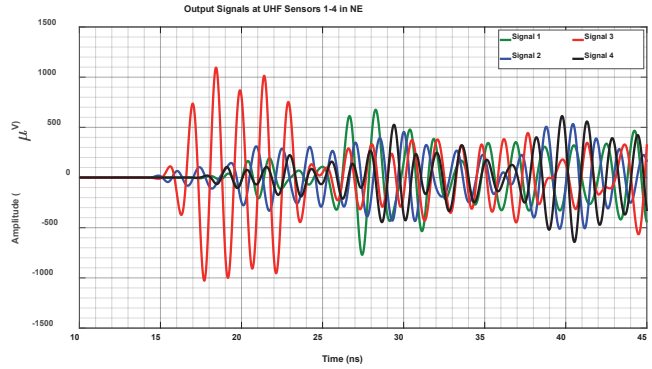

b)

Fig. 6. Output signals recorded at UHF sensors 1, 2, 3, and 4 for the transformer model filled with a) MO and b) NE. The sensors are represented by green, blue, red, and black curves, respectively.

Figures 6a and 6b present the simulated UHF sensor signals for the MO and NE transformer models, respectively, where the waveforms for sensors 1, 2, 3, and 4 are represented by green, blue,

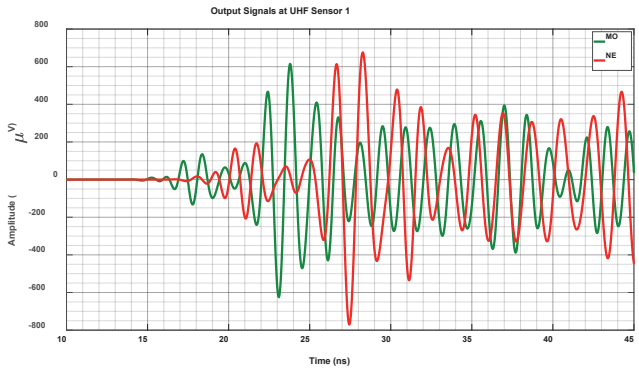

a)

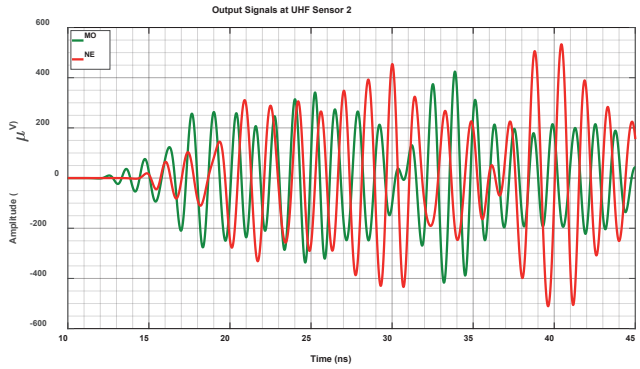

b)

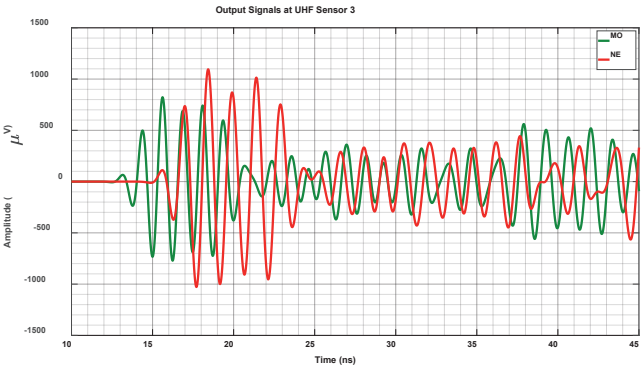

c)

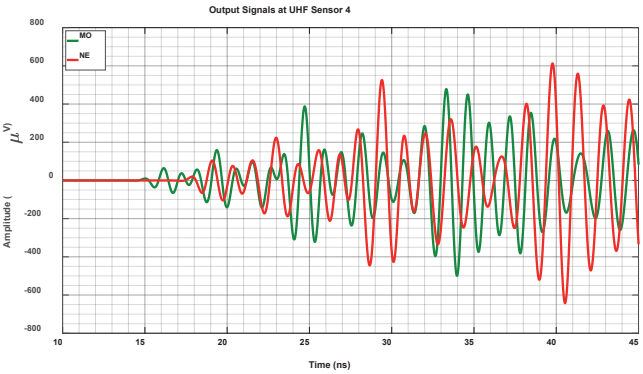

d)

Fig. 7. Comparison of output signals at UHF sensors a) 1, b) 2, c) 3, and d) 4 for the transformer model using MO (green) or NE (red).

Djordje Dukanac, Impact of Alternative Dielectric Liquids on UHF Partial Discharge Signal Propagation and Source Localization in Power Transformers, Journal of Energy, vol. 75 Number 3 (2026), 74–84
https://doi.org/10.37798/2026753790
© 2026 Copyright for this paper by authors. Use permitted under Creative Commons Attribution-NonCommercial (CC BY-NC) 4.0 International License

red, and black curves. Due to the lower relative permittivity of MO compared to NE, the PD signals propagate faster and reach the sensors earlier in the MO configuration.

Figures 7a–7d display the output signals recorded at UHF sensors 1–4, comparing the transformer models filled with MO (green curves) and NE (red curves). Compared to the MO configuration, the PD signals captured in the NE transformer model exhibit higher intensities and a distinct temporal delay, while maintaining structurally similar wave profiles with varying peak amplitudes.

Based on Figure 7c, the initial wave packet of the signal at sensor 3 has an approximate duration of 10 ns in both dielectric liquids; however, its exact onset time cannot be precisely determined. This early packet comprises PD signals traveling via direct or quasi-line-of-sight paths, which are heavily influenced by the geometry and density of intervening obstacles. Subsequently, the UHF sensors capture only indirectly propagated multipath components. Because the waveforms at sensors 1, 2, and 4 are characterized by more frequent and intense reflected waves, their transient transitions are significantly less pronounced than the sharp onset observed at sensor 3.

As illustrated in Figure 7, the extreme amplitudes (EAs) for Signals 1 and 4 in the NE-filled transformer model occur beyond the initial 10 ns wave packet, emerging at 10.721 ns and 12.179 ns relative to their respective first peaks (FPs). Consequently, this 12.179 ns window is established as the baseline reference interval for subsequent analyses to ensure these initial EAs are fully captured.

Figure 8a displays the plot of FP amplitude versus FP arrival time for the PD signals 1–4 received at the four UHF sensors. These signals originate from the same PD source within two power transformer models; one filled with MO and the other with NE. The data covers a 12.179 ns period starting from the signals' FPs, with the MO and NE results represented by green and red points, respectively.

The arrival sequence of the FPs is registered in the following chronological order: signal 2, signal 3, signal 1, and signal 4. Compared to the MO benchmark, the FPs in the NE transformer model exhibit distinct propagation delays and amplitude enhancements. Specifically, the FP arrival times for signals 1–4 are delayed by factors of 1.1921, 1.1895, 1.1916, and 1.1953, respectively. Furthermore, the corresponding FP amplitudes in the NE model are scaled up by factors of 1.8278, 1.6306, 1.8117, and 2.1298 relative to the MO configuration.

The amplitude and temporal relationships vary distinctively across both insulation domains. In the MO model, the FP of signal 3 is 4.194 and 7.234 times greater than those of signals 2 and 4, respectively, but drops below that of signal 1 by a factor of -8.78. For the NE model, these comparative factors shift to 4.659, 6.154, and -8.703, respectively. Temporally, signals 1, 2, and 3 consistently arrive ahead of signal 4. In the MO medium, these leading margins are 1.029 ns, 1.215 ns, and 1.157 ns, whereas in the NE medium, they are slightly tighter at 1.027 ns, 1.209 ns, and 1.153 ns.

For PD signals originating from a common internal source, Figure 8b illustrates the relationship between the EAs and their occurrence times. This evaluation is restricted to a 12.179 ns window relative to the signal FPs, with green and red data points denoting the MO and NE transformer insulation models, respectively.

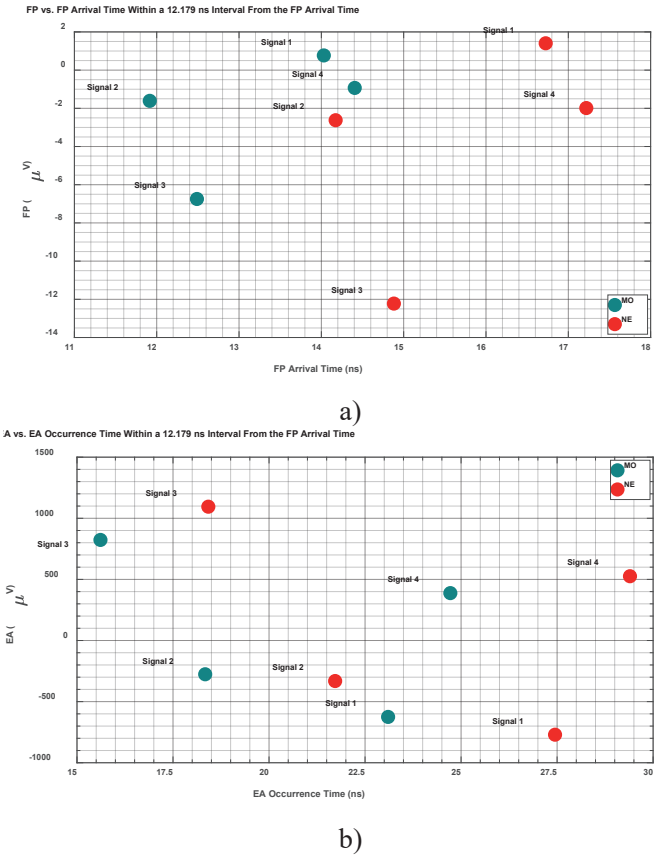

Fig. 8. Comparison of a) FP magnitude versus arrival time and b) EA magnitude versus occurrence time within a 12.179 ns window following the FPs. Green and red points represent the MO and NE transformer insulation models, respectively.

Figure 8b illustrates that within the 12.179 ns window relative to the signal FPs, the EAs register in the following chronological sequence: signal 3, signal 2, signal 1, and signal 4. Compared to the MO insulation model, the EAs in the NE configuration exhibit distinct propagation delays. Specifically, the EA occurrence times for signals 1–4 are delayed by scaling factors of 1.1882, 1.1845, 1.1799, and 1.1892, respectively.

Furthermore, the NE-to-MO ratios for the EA magnitudes of signals 1–4 are 1.2326, 1.2003, 1.3304, and 1.3561, respectively. However, when contrasted with the corresponding NE-to-MO FP ratios from Figure 8a, these relative values are reduced by factors of 1.4829, 1.3585, 1.3618, and 1.5705. This discrepancy implies that the amplification effect of multipath reflected waves over time is more pronounced in the MO medium than in the NE configuration.

In contrast to Figure 8a, where the FP of Signal 2 precedes that of Signal 3, Figure 8b demonstrates that the EA of Signal 3 occurs prior to that of Signal 2. This temporal shift indicates that intense multipath reflections dominate the Sensor 2 position. For the MO and NE configurations, the EA magnitude of Signal 3 varies relative to Signals 1, 2, and 4 by scaling factors of -1.317, -2.98, and 2.122, and -1.421, -3.302, and 2.082, respectively. Furthermore, the EA arrival of Signal 4 lags behind those of Signals 1, 2, and 3 by factors of 1.07, 1.348, and 1.584 in the MO environment, and 1.071, 1.353, and 1.596 under the NE configuration.

Figure 8 demonstrates that the signal waveforms in both models are structurally similar, but the NE model exhibits significantly higher magnitudes than the MO model.

Djordje Dukanac, Impact of Alternative Dielectric Liquids on UHF Partial Discharge Signal Propagation and Source Localization in Power Transformers, Journal of Energy, vol. 75 Number 3 (2026), 74–84
https://doi.org/10.37798/2026753790
© 2026 Copyright for this paper by authors. Use permitted under Creative Commons Attribution-NonCommercial (CC BY-NC) 4.0 International License

C. Spectral Diagrams of UHF Sensor Signals for MO and NE Models

Figures 9a and 9b display the S_{11} reflection coefficients of the PD source and the S_{21} transmission parameters to UHF Sensors 1–4 for the MO and NE transformer configurations, respectively.

Comparing the two liquid environments reveals a uniform shift toward higher frequencies across all S_{11} and S_{21} frequency response curves in the MO model relative to the NE model.

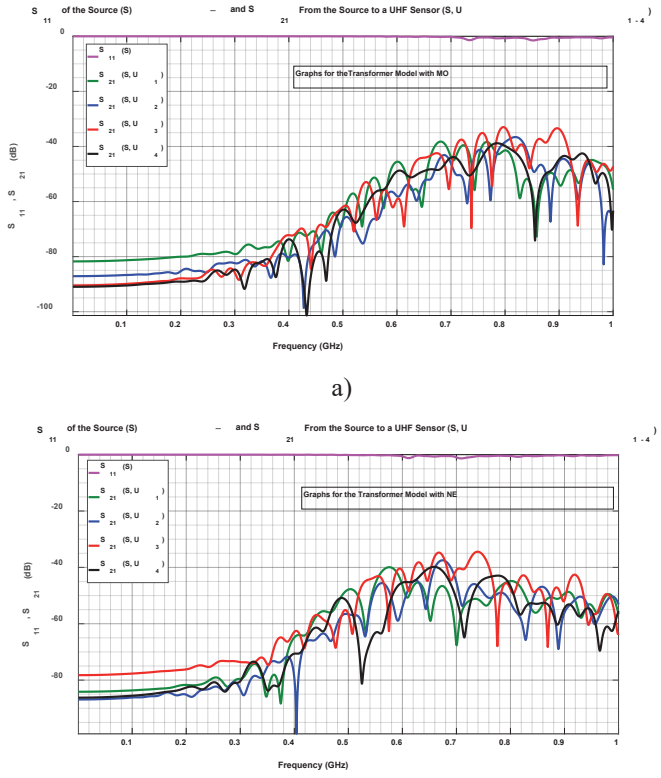

Fig. 9. Simulated S_{11} input reflection coefficients of the PD source and S_{21} transmission coefficients to UHF Sensors 1–4 for the transformer models configured with: a) MO, and b) NE.

Figure 10 displays the frequency-dependent S_{11} minima for the PD source alongside the S_{21} maxima for UHF Sensors 1–4. The green and red data points correspond directly to the results obtained from the MO and NE transformer configurations, respectively.

In Figure 2b, the peak radiated and accepted powers of the dipole antenna occur at 755 MHz for the MO cube and 630 MHz for the NE cube, establishing a baseline frequency ratio of 1.198. Consistent with this trend, Figure 10 demonstrates that the S_{11} minima and the S_{21} maxima for the signals at UHF Sensors 1–4 exhibit a clear upshift toward higher frequencies for the MO transformer model relative to the NE model. Specifically, the corresponding MO-to-NE frequency ratios calculated at UHF Sensors 1–4 are 1.202, 1.183, 1.078, and 1.193, respectively.

Figures 11a and 11b display the signal spectra for the MO transformer model within a 12.179 ns window following the FPs and from the FPs to the 45 ns record termination, respectively. Comparing these two intervals reveals that the peak spectral intensities of Signals 1 and 3 diminish in the late window, whereas the spectral maximum of Signal 4 intensifies during the interval extending from the FPs to the end of the simulation.

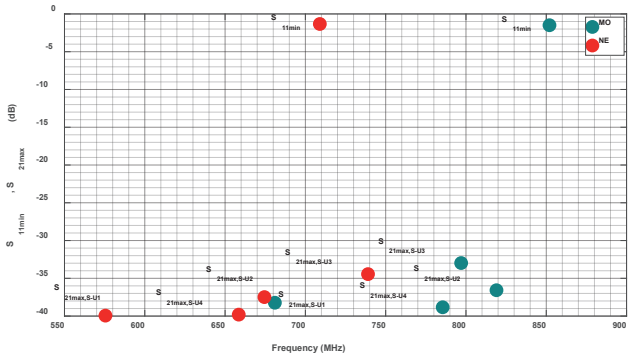

Fig. 10. Frequency-dependent S_{11} minima for the PD source and S_{21} maxima between the source and UHF Sensors 1–4. The green and red markers represent the results for the MO and NE transformer models, respectively.

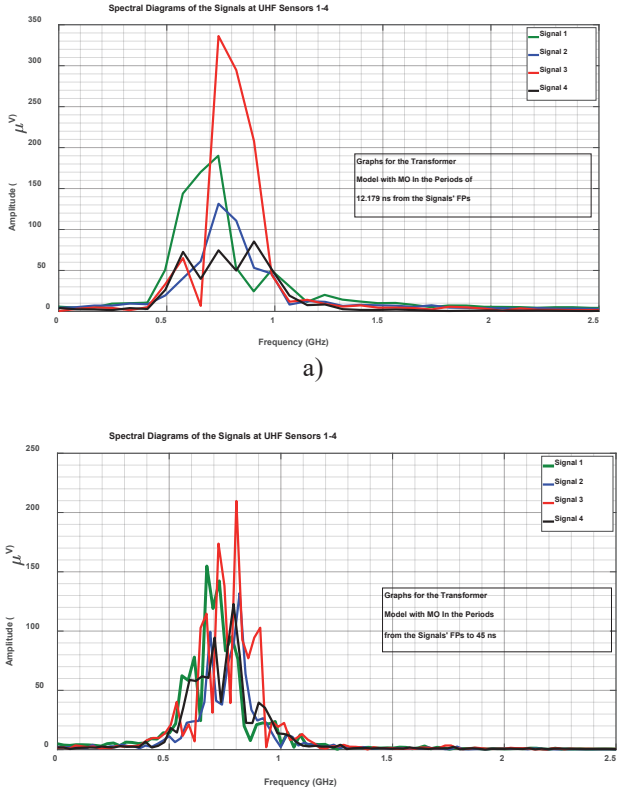

Fig. 11. UHF sensor signal spectra for the MO transformer model during time windows: a) up to 12.179 ns post-FP, and b) from the initial FPs to the end of the records. Green, blue, red, and black lines represent Signals 1, 2, 3, and 4, respectively.

Figures 12a and 12b display the signal spectra for the NE transformer model within a 12.179 ns window following the FPs and from the FPs to the 45 ns record termination, respectively. Comparing these two intervals reveals that the peak spectral intensity of Signal 3 attenuates significantly in the late window, whereas the spectral maxima of Signals 1, 2, and 4 intensify during the period extending from the FPs to the end of the simulation.

Djordje Dukanac, Impact of Alternative Dielectric Liquids on UHF Partial Discharge Signal Propagation and Source Localization in Power Transformers, Journal of Energy, vol. 75 Number 3 (2026), 74–84
https://doi.org/10.37798/2026753790
© 2026 Copyright for this paper by authors. Use permitted under Creative Commons Attribution-NonCommercial (CC BY-NC) 4.0 International License

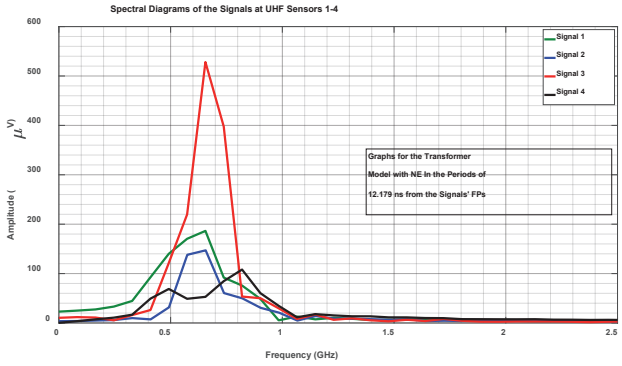

a)

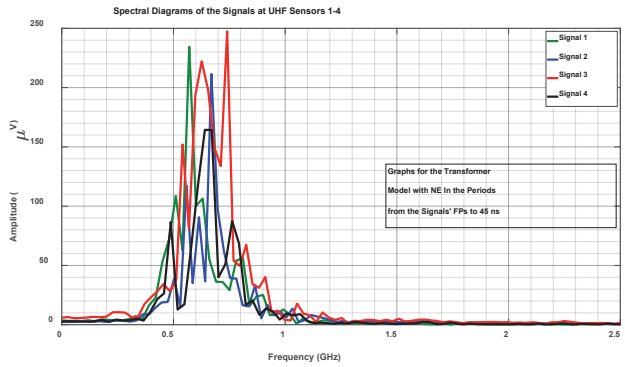

b)

Fig. 12. Spectral diagrams of the signals at UHF sensors 1–4 for the transformer model with NE during the intervals: a) up to 12.179 ns from the signal FPs, and b) from the FPs to the end of the 45 ns recording period. Signals 1, 2, 3, and 4 are plotted in green, blue, red, and black, respectively.

Figure 13 displays the weighted mean amplitudes versus the weighted mean frequencies extracted from the spectral diagrams of the signals at UHF sensors 1–4. These parameters are evaluated over two distinct intervals from the signal FPs: a shorter 12.179 ns window and the full period up to the end of the 45 ns recording. The results for the MO transformer model are plotted in green (shorter period) and light green (longer period), while those for the NE model are shown in red and purple, respectively.

When comparing the results for the transformer model with NE in Figure 13, Signals 3 and 1 exhibit the largest weighted mean amplitude ratios (shorter divided by longer time periods), measuring 1.777 and 1.616, respectively. In contrast, these ratios are lower for Signals 2 and 4, at 1.26 and 1.18, respectively. This indicates that, compared to sensors 2 and 4, the long-term effects of reflected waves on the received signals at sensors 3 and 1 are substantially reduced.

Based on the weighted mean frequency ratios (shorter divided by longer time periods) of 0.969, 1.015, 1.006, and 1.043, reflected waves only slightly alter the weighted mean frequencies of the signals. Specifically, Signal 1 shifts to the right by 18.736 MHz. In contrast, Signals 2, 3, and 4 shift to the left by 9.501 MHz, 4.009 MHz, and 27.856 MHz, respectively. Consequently, Signal 4 exhibits the largest overall frequency shift.

Based on the results in Figure 13 for the transformer model with MO, a comparison across the two post-FP evaluation intervals (shorter divided by longer time periods)—specifically, the initial 12.179 ns window versus the full duration up to 45 ns—reveals the highest weighted mean amplitude ratios for Signals 3, 1, and 2 (1.701, 1.412, and 1.398, respectively). Conversely, Signal 4 exhibits a much lower ratio of 1.032. This trend demonstrates that the long-term impact of reflected waves—which sustains signal amplitude over time—is most pronounced at sensor 4, while remaining minimal at sensor 3, followed by sensors 1 and 2.

Considering the ratios of the weighted mean frequencies between the shorter and longer time periods (defined as shorter/longer), which are 1.003, 1.015, 1.043, and 1.05, respectively, it can be concluded that reflected waves slightly shift the frequencies downward (to the left) over time. These leftward shifts measure 1.902 MHz, 11.42 MHz, 32.592 MHz, and 37.28 MHz for Signals 1 through 4, respectively, with the largest reductions occurring in Signals 4 and 3.

Comparing the results for the transformer models with NE and MO within 12.179 ns after the signal FPs, the weighted mean amplitude ratios (NE divided by MO) for Signals 1, 2, 3, and 4 are 1.276, 1.106, 1.504, and 1.381, respectively. These values demonstrate that the signals in the NE model reach larger weighted mean amplitudes than those in the MO model during this shorter period. Among the signals, Signal 3 exhibits the highest ratio, while Signal 2 shows the lowest.

Comparing the results for the transformer models with NE and MO from the signal FPs up to 45 ns, the weighted mean amplitude ratios (NE divided by MO) for Signals 1, 2, 3, and 4 are 1.115, 1.227, 1.439, and 1.207, respectively. These values demonstrate that the signals in the NE model consistently maintain larger weighted mean amplitudes than those in the MO model over this longer period. Among the signals, Signal 3 exhibits the highest ratio, whereas Signal 1 shows the lowest.

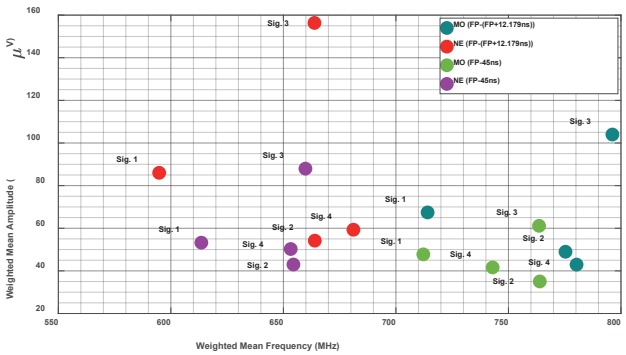

Fig. 13. Weighted mean amplitudes vs. weighted mean frequencies for Signals 1–4 at the corresponding UHF sensors based on their spectral diagrams. Results are shown for both evaluation intervals (12.179 ns and up to 45 ns after the signal FPs) across the transformer models filled with MO and NE.

The resulting double ratios—calculated by dividing the aforementioned weighted mean amplitude ratios (shorter divided by longer time periods) of the NE model by those of the MO model—are 1.144, 0.902, 1.045, and 1.144 for Signals 1, 2, 3, and 4, respectively. These values demonstrate that the relative deviation in the weighted mean amplitude ratios between the two dielectrics across both time periods ranges from −9.8% to 14.4% relative to unity.

When comparing the transformer models over the shorter, 12.179 ns interval following the signals' FPs, the MO model demonstrates consistently higher weighted mean frequencies than the NE model. Specifically, the MO-to-NE frequency ratios for signals 1 through 4 are 1.2005, 1.1678, 1.1994, and 1.1456, respectively. For the MO model, the weighted mean frequencies are 714.08 MHz, 775.35 MHz, 796.19 MHz, and 780.27 MHz, compared to 594.81 MHz, 663.96 MHz, 663.8 MHz, and 681.12 MHz for the NE model. Consequently, the weighted mean frequencies in the MO model are 14.56% to 20.05% higher than their corresponding values in the NE model.

Djordje Dukanac, Impact of Alternative Dielectric Liquids on UHF Partial Discharge Signal Propagation and Source Localization in Power Transformers, Journal of Energy, vol. 75 Number 3 (2026), 74–84
https://doi.org/10.37798/2026753790
© 2026 Copyright for this paper by authors. Use permitted under Creative Commons Attribution-NonCommercial (CC BY-NC) 4.0 International License

Over the extended period from the signals' FPs up to 45 ns, the MO model continues to show higher weighted mean frequencies than the NE model. The corresponding MO-to-NE ratios for signals 1 through 4 are 1.1608, 1.1673, 1.1573, and 1.1374, respectively. In this timeframe, the MO model yields frequencies of 712.18 MHz, 763.93 MHz, 763.6 MHz, and 742.99 MHz, whereas the NE model results in 613.54 MHz, 654.46 MHz, 659.79 MHz, and 653.26 MHz. Consequently, the weighted mean frequencies are 13.74% to 16.73% higher in the MO model relative to the NE model.

For both the shorter and longer periods, the peak radiated and accepted powers of the dipole antenna (found at 630 MHz for the NE cube and 755 MHz for the MO cube in Figure 2b fall within the calculated ranges of the corresponding weighted mean frequencies shown in Figure 13. These frequencies were obtained from the transformer model in Figure 1a, which is filled with MO and NE separately. Furthermore, evaluating the data from Figure 13, the resulting double ratios calculated by dividing the shorter-period weighted mean frequency ratios by their longer-period counterparts of the MO model by those of the NE model yield values of 1.0343, 1.0004, 1.0364, and 1.0072 for signals 1 through 4, respectively. These results indicate that the variance in the weighted mean frequency ratios remains minimal for the shorter time period relative to the longer time period, spanning a narrow range of 0.04% to 3.64% across the evaluated signals.

D. PD Source Localization in the Two Alternative Liquid Dielectrics

Because a system of four nonlinear equations with four unknown variables can be generated and solved, four sensors are sufficient for the precise localization of a PD source [3], [6].

The TDOAs between the FPs of the respective signals at three UHF sensors, relative to the signal at the fourth reference UHF sensor, were calculated using the FP method. By examining the recorded signals in Figures 6 and 7, the three TDOAs can be identified for each transformer model—specifically, the first model with MO and the second with NE.

The time of arrival of the signal at the reference sensor and the three spatial coordinates of the PD source site represent the four unknown values to be determined in the FP method. These equations incorporate fixed parameters, including the 3D positions of the UHF sensors and the propagation velocity of the UHF signal, which is 20.23 cm/ns in MO and 16.77 cm/ns in NE. To maximize the TDOAs between sensors, adjacent UHF sensors should generally be positioned as far apart as possible.

The bar graph in Figure 14a displays, from left to right, the TDOAs for sensor pairs 2–1, 3–1, and 4–1, using signal 1 as the reference. The MO and NE transformer models are represented by green and red bars, respectively. The data reveal unequal TDOA variations between the models, with the NE model consistently exhibiting larger absolute values. Specifically, the deviations across these successive pairs are -0.4373 ns, -0.3027 ns, and 0.1177 ns. These variations directly propagate into the final PD source localization results.

Pair 2–1 exhibits the maximum absolute deviation of -0.4373 ns because U_2 is physically positioned roughly 50 cm closer to the source than U_1, amplifying the time-saving delta when the propagation velocity decelerates from 20.23 cm/ns in MO to 16.77 cm/ns in NE. A similar baseline applies to pair 3–1 due to a 41.39 cm path advantage for U_3. Conversely, U_4 and U_1 exhibit structural symmetry relative to the source coordinates, yielding a minimal spatial delta of roughly 3.35 cm and a negligible positive TDOA shift of 0.1177 ns. The minor variation between ideal line-of-sight metrics and these observed values represents the cumulative propagation delays induced by diffraction and multipath reflections around the simplified winding geometries. When processed, these asymmetric temporal distortions misalign the hyperbolic space intersections, directly precipitating the localization error inflation observed in the NE model.

Figure 14b shows the calculated average absolute localization errors of the PD source for both dielectric liquids. The green and red points represent the MO and NE models, respectively. Using NE results in a larger localization error, exceeding the MO model by 1.017 mm.

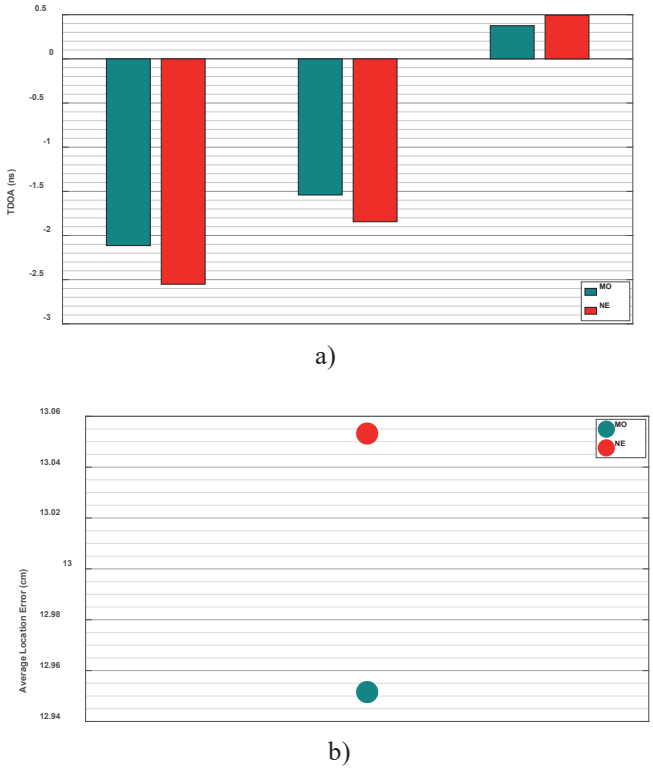

Fig. 14. PD source localization performance for MO and NE transformer models: a) TDOAs of signals 2, 3, and 4 relative to reference signal 1; b) average absolute location errors, indicated by green (MO) and red (NE) data points.

IV. Discussion

The results align with the physical mechanisms governing UHF PD EM wave propagation. Specifically, the responses at Sensors 1–4 are dictated by the configured dielectric liquid properties.

The higher relative permittivity (ε_r) of NE compared to MO introduces several critical physical effects within the transformer models:

- Decelerates the UHF signal propagation velocity from 20.23 cm/ns in MO down to 16.77 cm/ns in NE.
- Intensifies boundary reflections and decreases wave diffraction at metallic interfaces, distorting the original pulse shape and the received sensor waveforms.
- Enhances the capacitive coupling at the PD source, promoting greater charge separation within the discharge streamer. This intensified charge dynamics, combined with the lower streamer velocity characteristic of NE, generates a highly energetic EM radiated emission baseline. Consequently, this elevated

Djordje Dukanac, Impact of Alternative Dielectric Liquids on UHF Partial Discharge Signal Propagation and Source Localization in Power Transformers, Journal of Energy, vol. 75 Number 3 (2026), 74–84
https://doi.org/10.37798/2026753790
© 2026 Copyright for this paper by authors. Use permitted under Creative Commons Attribution-NonCommercial (CC BY-NC) 4.0 International License

initial radiation energy ensures that the transient UHF EM waves arriving at the sensors remain systematically stronger in the NE model than in the MO model.

While the higher dielectric loss tangent (*tanδ*) of NE promotes greater signal attenuation along the propagation path, its elevated relative permittivity amplifies the initial discharge energy at the PD source. This heightened source intensity more than compensates for the medium's increased signal absorption, ensuring that the net transient amplitudes arriving at the sensors remain systematically stronger in the NE transformer model than in the MO model under identical excitation profiles.

The higher mass density (ρ) of NE retards rapid charge mobility during the pre-breakdown phase. This spatial inhibition concentrates the localized energy, culminating in a more violent, high-peak-energy discharge before the streamer traverses the oil gap—a phenomenon that becomes critically pronounced under elevated thermal conditions.

V. Conclusion

This paper utilizes 3D Ansys HFSS simulations to analyze PD EM wave propagation and evaluate source localization accuracy within a power transformer. The model simulates PD transmission from a dipole antenna source through internal metal windings to four UHF sensors, comparing performance across MO and NE dielectrics. To account for the complex reflections and diffractions caused by internal geometric obstacles, the simulation extracts and plots the received sensor signals on a nanosecond (ns) time scale.

The main conclusions of this paper are:

- Within the cube enclosure, the center-mounted antenna achieves a peak far-field realized gain of 3.96 dB across the 2D rectangular contours with NE, marking a 0.8 dB improvement over the 3.16 dB peak observed with MO.
- Comparison of the liquid dielectrics within the standard transformer model reveals distinct propagation behaviors within a 12.179 ns window following the FP arrival times. Specifically, the FPs and EAs of signals 1–4 are 1.6306 to 2.1298 times and 1.2003 to 1.3561 times larger in the NE model than in the MO model, respectively. This trend demonstrates that multipath reflections amplify more rapidly over time within the MO environment, whereas the NE environment suppresses late-stage scattering, thereby maintaining the integrity of early signal components.
- Comparing the shorter period (12.179 ns post-FP) against the extended observation window (up to 45 ns) yields the following insights:
- Comparing the transformer models, the NE model exhibits significantly higher weighted mean amplitudes than the MO model across both time windows. Their amplitude ratios (NE/MO) range from [1.106–1.504] in the shorter period to [1.115–1.439] in the longer period.
- The MO model yields higher weighted mean frequencies than the NE model in both periods. The MO/NE ratios range from [1.1456–1.2005] in the shorter period to [1.1374–1.1673] in the longer period.
- The peak radiated and accepted powers of the dipole antenna 630 MHz for NE and 755 MHz for MO cubes consistently align with the weighted mean frequencies of the signals captured by UHF Sensors 1–4 across all observation intervals. Additionally, the S_{11} reflection and S_{21} transmission profiles display a uniform frequency upshift in the MO transformer model compared to the NE model. This confirms that the baseline EM behaviors established in the basic cube configuration successfully scale to a complex, full-scale power transformer environment.
- Absolute TDOA metrics are consistently higher in the NE model compared to the MO environment, with deviations ranging between 0.1177 ns (sensors 4–1) and -0.4373 ns (sensors 2–1). Consequently, these timing discrepancies propagate into the localization algorithm, causing a 1.017 mm increase in PD source localization error for the NE transformer relative to the MO configuration.

In contrast to laboratory testing or in-service monitoring, this numerical simulation assumes idealized conditions. While UHF background noise is low in practice, real-world RF interferences are omitted here. Additionally, this framework bypasses hardware timing constraints like oscilloscope digitization limitations; the temporal resolution of the transient wavefront is dictated solely by the discrete solver time-step.

While this study lacks direct experimental validation on an identical prototype, executing such testing presents major practical limitations. It requires inserting a PD source —such as a high-power pulse generator or a transmitting antenna—within the winding assembly and sequentially replacing the tank's dielectric liquids. Additionally, fixed physical hatches prevent dynamic realignments of the UHF sensors with the principal EM wave vectors. Similar experimental validation frameworks are detailed extensively in the cited references.

Unlike idealized models where a PD source is assumed to be an omnidirectional point source, real-world in-service PD characteristics are unknown. Furthermore, this Ansys HFSS model introduces specific geometric simplifications by abstracting the HV/LV windings and omitting non-critical components. Because both the PD source and UHF sensors are modeled as dipole antennas, the simulated source lacks uniform omnidirectional radiation. This directional variance modifies the captured signal profiles and amplitudes across sensor channels relative to actual physical occurrences.

Ultimately, these 3D simulations serve as an effective tool to analyze the time-domain and spectral characteristics of low-intensity PD signals across the four UHF sensors. The virtual environment eliminates experimental variability by enabling precise source placement to directly quantify localization algorithm errors. Consequently, it allows for a highly controlled, repeatable comparison of the sensor array responses across both dielectric liquids under identical structural conditions.

The transient waveforms at Sensors 1–4 share structural similarities across both transformer models, yet their spectral and temporal profiles differ markedly. The NE model yields higher spectral amplitudes and a distinct downward frequency shift compared to the MO environment. Within a 12.179 ns window past the initial FP arrival, both the FPs and EAs exhibit larger magnitudes and systematic delays under the NE configuration. From an operational monitoring standpoint, these amplified signals enhance the signal-to-noise ratio, making PD detection easier in NE-insulated transformers. Nevertheless, because the higher permittivity of NE decelerates wave propagation and delays multipath arrivals, these increased signal magnitudes do not yield higher spatial accuracy during geometric localization.

Djordje Dukanac, Impact of Alternative Dielectric Liquids on UHF Partial Discharge Signal Propagation and Source Localization in Power Transformers, Journal of Energy, vol. 75 Number 3 (2026), 74–84
https://doi.org/10.37798/2026753790
© 2026 Copyright for this paper by authors. Use permitted under Creative Commons Attribution-NonCommercial (CC BY-NC) 4.0 International License

References

[1] D. Dukanac, "Extraction of partial discharge signal in predominant VHF range in the presence of strong noise in power transformer," *Electrical Engineering*, vol. 105, no. 5, pp. 3001–3018, May 2023, doi: 10.1007/s00202-023-01855-x.

[2] D. Dukanac, "Detection and analysis of a partial discharge signal in the power transformer using UHF method (in Serbian)," *Energy, Economy, Ecology*, vol. XXII, no. 1-2, pp. 96–101, Dec. 2020, doi: 10.46793/EEE20-1-2.096D.

[3] D. Dukanac, "Application of UHF method for partial discharge source location in power transformers," *IEEE Transactions on Dielectrics and Electrical Insulation*, vol. 25, no. 6, pp. 2266–2278, Dec. 2018, doi: 10.1109/TDEI.2018.006996.

[4] D. Dukanac, "Locating Partial Discharges in a Power Transformer Using UHF Technique (in Serbian)," *Energy, Economy, Ecology*, vol. XXIII, no. 2, pp. 73–78, Mar. 2021, doi: 10.46793/EEE21-2.73D.

[5] C. P. Beura, J. Wolters, S. Tenbohlen, "Application of Pathfinding Algorithms in Partial Discharge Localization in Power Transformers," *Sensors*, vol. 24, no. 2, 14 pages, Jan. 2024, Art. no. 685, doi: 10.3390/s24020685.

[6] F. Khodaveisi, H. Karami, M. Z. Karimpour, M. Rubinstein, F. Rachidi, "Partial discharge localization in power transformer tanks using machine learning methods," *Scientific Reports*, vol. 14, 13 pages, May 2024, Art. no. 11785, doi: 10.1038/s41598-024-62527-9.

[7] C. P. Beura, M. Beltle, S. Tenbohlen, M. Siegel, "Quantitative Analysis of the Sensitivity of UHF Sensor Positions on a 420 kV Power Transformer Based on Electromagnetic Simulation," *Energies*, vol. 13, no. 1, 17 pages, Dec. 2019, Art. no. 3, doi: 10.3390/en13010003.

[8] C. P. Beura, M. Beltle, P. Wenger, S. Tenbohlen, "Experimental Analysis of Ultra-High-Frequency Signal Propagation Paths in Power Transformers," *Energies*, vol. 15, no. 8, 15 pages, Apr. 2022, Art. no. 2766, doi: 10.3390/en15082766.

[9] T. Umemoto, S. Tenbohlen, "Validations of simulation of UHF electromagnetic wave propagation in an oil-filled tank by time-domain measurements," *IET Generation, Transmission & Distribution*, vol. 13, no. 9, pp. 1646–1652, Apr. 2019, doi: 10.1049/iet-gtd.2018.6173.

[10] L. A. M. M. Nobrega, E. G. Costa, A. J. R. Serres, G. V. R. Xavier, M. V. D. Aquino, "UHF Partial Discharge Location in Power Transformers via Solution of the Maxwell Equations in a Computational Environment," *Sensors*, vol. 19, no. 15, Aug. 2019, Art. no. 3435, doi: 10.3390/s19153435.

[11] M. A. Jangjoo, M. Allahbakhshi, H. R. Mirzaei, A. Abooee, "Partial Discharge Localisation in Power Transformer by UHF Technique," *High Voltage*, vol. 10, no. 5, pp. 1314–1323, May 2025, doi: 10.1049/hve2.70022.

[12] Z. Ma, L. Cai, D. Zhou, A. Wen, S. Jiang, C. Lin, Y. Wang, "A Study on the Enhanced Extraction of Ultra-High-Frequency Signals Induced by Transformer Core Coupling," *Energies*, vol. 18, no. 22, 15 pages, Nov. 2025, Art. no. 5903, doi: 10.3390/en18225903.

[13] N. Xue, J. Yang, D. Shen, P. Xu, K. Yang, Z. Zhuo, L. Zhang, J. Zhang, "The Location of Partial Discharge Sources Inside Power Transformers Based on TDOA Database with UHF Sensors," *IEEE Access*, vol. 7, pp. 146732–146744, Oct. 2019, doi: 10.1109/ACCESS.2019.2945893.

[14] S. Zheng, C. Li, Z. Tang, W. Chang, M. He, "Location of PDs inside transformer windings using UHF methods," *IEEE Transactions on Dielectrics and Electrical Insulation*, vol. 21, no. 1, pp. 386–393, Feb. 2014, doi: 10.1109/TDEI.2013.003863.

[15] T. Jiang, J. Li, Z. He, P. Wang, "Simulation and experiments of UHF detection for partial discharge in power transformers," in *2013 Annual Report Conference on Electrical Insulation and Dielectric Phenomena*, Shenzhen, China, 2013, pp. 1262–1265, doi: 10.1109/CEIDP.2013. 6748240.

[16] L. A. M. M. Nobrega, G. V. R. Xavier, M. V. D. Aquino, A. J. R. Serres, C. C. R. Albuquerque, E. G. Costa, "Design and Development of a Bio-Inspired UHF Sensor for Partial Discharge Detection in Power Transformers," *Sensors*, vol. 19, no. 3, Feb. 2019, Art. no. 653, doi: 10.3390/s19030653.

[17] D. Dukanac, "Analysis of the Influence of Active Parts of the Power Transformer on the Propagation of Signals from Source of Partial Discharges to UHF Sensors (in Serbian)," *Energy, Economy, Ecology*, vol. XXIV, no. 1, pp. 74–80, 2022, doi: 10.46793/EEE22-1.74D.

[18] D. Dukanac, "Power Transformer Numerical Modeling to Locate Partial Discharge Source Using the UHF Technique," *B&H Electrical Engineering*, vol. 17, no. 2, pp. 24–31, Nov. 2023, doi: 10.2478/bhee-2023-0009.

[19] D. Dukanac, "Influences of Reflections and Diffractions of Waves and the Modelled Source and UHF Sensors When Locating Partial Discharges in a Power Transformer (in Serbian)," *Energy, Economy, Ecology*, vol. XXVI, no. 3, pp. 11–20, Sep. 2024, doi: 10.46793/EEE24-3.11D.

[20] D. Dukanac, "Dependence of UHF Partial Discharge Detection and Source Positioning in Power Transformers on Different Input Pulse Frequency Ranges," *B&H Electrical Engineering*, ahead of print, 10 pages, Feb. 2026, doi: 10.2478/bhee-2026-0019.

© 2026 Copyright for this paper by authors. Use permitted under Creative Commons Attribution-NonCommercial (CC BY-NC) 4.0 International License